

# Spatial and temporal variability in Hawaiian hotspot volcanism induced by small-scale convection

Maxim D. Ballmer<sup>1,2,\*</sup>, Garrett Ito<sup>1</sup>, Jeroen van Hunen<sup>3</sup>, and Paul J. Tackley<sup>2</sup>

(1) School of Ocean and Earth Sciences and Technology, University of Hawaii, Honolulu, USA

(2) Institute of Geophysics, ETH Zürich, Zürich, Switzerland

(3) Department of Earth Sciences, Durham University, Durham, UK

(\*) corresponding author: ballmer@hawaii.edu

## Supplemental Information

### SA. Methods

In order to discretize and solve the equations of conservation of mass, momentum and energy, we use an extended version of the finite element code Citcom<sup>31,32</sup>. The most important extensions include formulations for compositional rheology (Eq. S3), and compositional buoyancy (Eq. S4), both being sensitive to partial melting processes. Related time-dependent feedback mechanisms between consumption of latent heat of fusion  $L$ , buoyancy, partial melting and rheology require application of the extended Boussinesq approximation<sup>33</sup> and of a 2nd-order Runge-Kutta time-integration scheme<sup>34,35</sup>. Details of the numerical method used are described elsewhere<sup>21,35</sup>.

The Cartesian model box spans dimensions 4818x3300x660 km (Fig. 1) with 672x384x96 rectangular elements, and element sizes ranging from 8.4x9.9x6.6 km to 4.6x4.3x3.4 km. An imposed, constant horizontal motion on the top boundary simulates 80 km/Myr of Pacific plate-motion<sup>36</sup>. In order to accommodate this motion, one vertical side of the box is free to inflow and the opposite side to outflow. The other sides are closed. The bottom is also closed except for a small circular region of radius of  $4r_p$  ( $r_p = 68$  km) wide enough to allow a mantle plume to rise into the box, and centered 3135 km downstream from inflow boundary. At the same location, a Gaussian thermal anomaly of amplitude  $T_p$  and of half-width  $r_p$  is imposed to supply excess temperature to the plume<sup>4</sup>. Otherwise, temperatures at the top and bottom remain fixed at 0 °C and the reference temperature  $T_m = 1350$  °C, respectively. On the inflow boundary, temperatures are maintained based on a simple cooling profile for 50 Myr-old lithosphere plus an adiabatic gradient  $\gamma = 0.3$  K/km and a random thermal noise of  $\pm 5$  °C.

In order to simulate melting of a heterogeneous mantle, we apply the marble cake mantle hypothesis<sup>28,37,38</sup>. Accordingly, we assume that the mantle is compositionally heterogeneous on a scale smaller than the finite element mesh. We take a marble cake recipe of biminerally silica-deficient pyroxenite (PX; cf. ref. 27) making up  $\Phi_{PX} = 5\%$  of

the mass of the mantle<sup>39</sup>, and of two flavors of peridotite: a depleted component (DC) for dry peridotite and a hydrous component (HC) for peridotite with high volatile content (we model a bulk water content  $c_0 = 0.03$  wt.-%, and no CO<sub>2</sub> content for simplicity) with  $\Phi_{DC} = 80\%$  and  $\Phi_{HC} = 15\%$ . We neglect any larger-scale heterogeneity, except for that PX is restricted to the plume. The radius of the compositional plume is fixed at  $r_P$ , outside of which  $\Phi_{PX}$  is initially 0%. Our model results are however independent of this restriction.

Each of these lithologies has a distinct melting behavior. HC and PX start melting significantly deeper (or at lower temperatures) than DC with PX clearly having the highest melt productivity. In order to simulate melting of PX and DC, we use the parametrizations of *Pertermann and Hirschmann*<sup>40</sup>, and *Hirschmann et al.*<sup>41</sup>, respectively. We apply the dynamic melting approximation for each lithology individually: melt accumulates in small pores in any lithology until a critical porosity  $\varphi_C$  is reached, beyond which melt is assumed to be extracted instantaneously to maintain the porosity at  $\varphi_C$  in that lithology<sup>42</sup>. In most of our cases we take  $\varphi_C = 1\%$ , but we also vary  $\varphi_C$  between 0.5% and 0.9% (cf. Suppl. Inf. SC). For HC, we reduce melting temperatures relative to DC by  $\Delta T_{sol}$  according to the hydrous peridotite melting parametrization of *Katz et al.*<sup>43</sup>:

$$\Delta T_{Sol} = K \left( \frac{c_{HC}}{D_{H2O}} \right)^{0.75} \quad (S1)$$

with the bulk distribution coefficient for water  $D_{H2O} = 0.01$ , and  $K = -43$  wt.-%<sup>-0.75</sup>K. When the depletion (i.e., extent of melting) in HC,  $F_{HC}$ , exceeds  $\varphi_C$ , the water content in the HC solid residue  $c_{HC}$  is efficiently reduced by melt extraction according to *Zou*<sup>44</sup>:

$$c_{HC} = c_0 \frac{D_{H2O} \left( 1 - \frac{F_{HC} - \varphi_C}{1 - \varphi_C} \right)^{\frac{1}{\varphi_C + (1 - \varphi_C) D_{H2O}} - 1}}{F + D_{H2O} (1 - F_{HC})} \quad (S2)$$

Consequently, the altered water content of the solid affects the solidus (cf. equation S1).

As olivines in DC and HC dominate the rheology of the lithological assemblage (since  $\Phi_{DC} + \Phi_{HC} = 95\%$ ), we apply an experimentally calibrated olivine rheology<sup>45-47</sup>. An activation energy of  $E^* = 300$  kJ/mol<sup>45</sup> leads to strong temperature dependence of viscosity. We also include compositional effects such as melt lubrication<sup>48</sup>, and more importantly, stiffening due to dehydration of the solid with ongoing depletion in HC<sup>46</sup>:

$$\eta = \eta_m \left( \frac{\zeta(c_0 - c_{dry})}{\zeta(c_{HC} - c_{dry}) + c_0 - c_{HC}} \right)^{\Phi_{EC}} \exp \left( \frac{E^* + \rho_m g z V^*}{RT} - \frac{E^*}{RT_m} - \zeta(\Phi_{DC} \varphi_{DC} + \Phi_{HC} \varphi_{HC}) \right) \quad (S3)$$

**Table S1: Notations.**

parameter	description	value or range; unit
$c_{dry}$	water concentration in the solid HC, below which hydrous olivine behaves like dry olivine	6 wt.-ppm
$c_{HC}$	water concentration in the solid HC	[wt.-ppm]
$c_O$	initial water concentration in the solid HC	300 wt.-ppm
$E^*$	activation energy	$3 \cdot 10^5$ J/mol
$F_{DC}$	depletion in DC	-
$F_{HC}$	depletion in HC	-
$g$	gravity acceleration	$9.8 \text{ kg/s}^2$
$L$	latent heat of fusion	$5.6 \cdot 10^5$ J/kg
$p$	lithostatic pressure	[Pa]
$r_P$	radius of the plume	68 km
$T$	temperature	[K]
$T_m$	mantle potential temperature	1350 °C
$T_P$	plume potential temperature	1650 °C
$T_{sol}$	dry solidus temperature	[K]
$V^*$	activation volume	$5 \cdot 10^{-6} \text{ m}^3/\text{mol}$
$\alpha$	thermal expansivity	$3 \cdot 10^{-5} \text{ K}^{-1}$
$\gamma$	adiabatic gradient	0.3 K/km
$\Delta T_{sol}$	hydrous solidus reduction	[K]
$\Delta \rho_F$	density anomaly related to 100% depletion in peridotite	$-165 \text{ kg/m}^3$
$\Delta \rho_\phi$	density anomaly related to 100% melting	$-500 \text{ kg/m}^3$
$\zeta$	melt lubrication exponent	40
$\eta$	viscosity	[Pa·s]
$\eta_{eff}$	effective mantle viscosity	$1.8 \cdot 10^{19} \text{ Pa}\cdot\text{s}$
$\xi$	dehydration stiffening coefficient	310.6383
$\rho_0$	reference mantle density	$3300 \text{ kg/m}^3$
$\phi_C$	critical porosity	0.5-1.0 %
$\phi_{DC}, \phi_{HC}, \phi_{PX}$	porosities in DC, HC and PX ( <i>respectively</i> )	-
$\Phi_{DC}$	mass fraction of DC	80%
$\Phi_{HC}$	mass fraction of HC	15%
$\Phi_{PX}$	initial mass fraction of PX	5%

with  $R$ ,  $\eta$ ,  $\eta_m$ ,  $\phi_{DC}$ ,  $\phi_{HC}$ ,  $\xi$ ,  $\zeta$ ,  $V^*$ ,  $\rho_m$ ,  $g$ ,  $z$ ,  $T$ ,  $T_m$ , and  $c_{dry}$  the ideal gas constant, viscosity, reference mantle viscosity, porosity in DC, porosity in HC, dehydration stiffening coefficient, melt lubrication coefficient, activation volume, reference mantle density, gravity acceleration, depth, temperature, and the water content below which hydrous olivine behaves like dry olivine, respectively (see Table S1 for values). The effective viscosity  $\eta_{eff} \equiv 0.00155\eta_m$  corresponds to the minimum viscosity in the upper mantle column at the onset of small-scale convection (SSC), and is a better representation for the rheology of the ambient mantle than  $\eta_m$ . The dehydration stiffening coefficient  $\xi$  is scaled such that dehydrating HC from  $c_{HC} = 100$  ppm to  $c_{HC} = c_{dry}$  increases the viscosity of HC by a factor of 100 (ref. 47). Substituting equation (S2) into equation (S3) elucidates that rheology is dependent on variables  $T$ ,  $z$ ,  $F_{HC}$ , and  $\phi_{HC}$  only.

Lateral density variations, which drive convection, depend on temperature, bulk porosity  $\varphi$  (with  $\varphi = \varphi_{DC}\Phi_{DC} + \varphi_{HC}\Phi_{HC} + \varphi_{PX}\Phi_{PX}$ ) and depletion in peridotite:

$$\rho - \rho_m = \alpha\rho_m(T - T_m) + \Delta\rho_\varphi\varphi + \Delta\rho_F(\Phi_{DC}F_{DC} + \Phi_{HC}F_{HC}) \quad (\text{S4})$$

with  $\Delta\rho_\varphi$ ,  $\Delta\rho_F$ ,  $\alpha$ ,  $\rho$ ,  $F_{DC}$ , and  $\varphi_{PX}$  the density changes with melt retention and peridotite depletion, thermal expansivity, density, depletion in DC, and porosity in PX, respectively. We ignore the small density variations related to the consumption of PX by melting, since the density of pyroxenite is close to that of the mantle, and since  $\Phi_{PX}$  is just 5%.

### SB. Controls on plume-pancake SSC and related effects on volcanism

As opposed to SSC in the ambient mantle self-organizing as regularly spaced, linear rolls parallel to plate motion, SSC in the hot plume pancake is more complex in flow geometries (cf. ref. 24). In both places, SSC rolls are aligned according to the differential motion between the low-viscosity mantle and the overriding plate<sup>49</sup>. Whereas this differential motion is dominated by the plate motion in the ambient mantle, it is strongly affected by the gravitational spreading of the plume in the pancake. Figure S1 shows the horizontal flow at a depth of 140 km minus 80 km/Myr of plate motion. The overall differential flow radiates outward away from the plume stem. Directly downstream of the plume stem, gravitational spreading drives flow that is parallel to but faster than plate motion; far away from the axis of the hypothetical hotspot track, gravitational spreading results in a strong component of flow perpendicular to plate motion. Accordingly, SSC rolls tend to align parallel to plate motion along the central axis of the plume pancake, and perpendicular to plate motion on the flanks of the pancake (Fig. S1).

Plume-pancake SSC controls locations of decompression melting and related secondary volcanism. Stable upwellings directly downstream of the hotspot oriented parallel to plate motion give rise to rejuvenated stage volcanism. Transient upwellings (cf. movie supplement) on the distal flanks of the pancake (oriented perpendicular to plate motion) spawn arch volcanism ~300 km away from the central axis of the hypothetical island chain. Another type of arch volcanism is predicted to emerge ~250 km upstream of the hotspot above a localized upwelling of plume-pancake SSC. This upwelling is triggered by a nearby downwelling of ambient-mantle SSC that carves into the plume pancake to focus the otherwise diffuse flow (Fig. S2).

The predicted sites and volumes agree well with the observed geographic distributions of rejuvenated stage volcanism, and arch volcanism around Hawaii. In particular, our models display a near-gap between the hotspot and the rejuvenated melting zones of ~80 km (cf. Fig. 3b) that addresses the observed gap of 1-2 Myrs<sup>17,18,50</sup> between the shield and rejuvenated phases of Hawaiian volcanism. In addition, a length-scale of

~300 km for the rejuvenated melting zone can readily explain occurrences of coeval rejuvenated volcanism on Niihau and Maui<sup>16-18,50</sup>. In terms of arch volcanism, the models predict volcanic fluxes as high as ~1000 km<sup>3</sup>/Myr occurring ~300 km away from the central axis of the island chain, fluxes and locations that are consistent with observations for the Hawaiian North Arch Volcanic Field<sup>19</sup> (cf. Fig. 1a). Predicted arch volcanism occurring 200-300 km upstream of the hotspot displays a smaller volume flux (~25 km<sup>3</sup>/Myr) and can thus account for the South Arch Volcanic Field<sup>20</sup>. The precise patterns of secondary volcanism however may be influenced by various mechanisms not modelled. These may include a possible recent change in Pacific plate motion<sup>51</sup>, associated complications in the pattern of SSC<sup>52</sup>, localized intermediate-scale fertile anomalies in the mantle source<sup>10</sup>, and lateral flow of magma.

The importance of ambient-mantle SSC for the symmetry of flow and temperature in the plume pancake as well as for the occurrence of secondary volcanism is explored by comparing the predictions of the reference case (Fig. S2a) with a case that has ambient-mantle SSC artificially switched off (Fig. S3). The latter case is governed by the same model parameters as the first, and differs only in the length of the box in the direction of plate motion, which is just 2376 km, instead of 4818 km for the first. Such a short box does not allow enough time for ambient-mantle SSC to organize upstream of the plume. The large-scale pattern of temperature and flow in the plume pancake are similar for both the reference case (Fig. S2a) and the short-box case (Fig. S3a), independent of the occurrence of ambient-mantle SSC. However, the pancake is much more symmetric in the short-box case because there are no pre-existing undulations in lithospheric thickness (“washboard”-pattern) to trigger asymmetric flow. Likewise, the pyroxenite contribution in hotspot volcanism (Fig. S3b) and the pattern of plume-pancake SSC are almost completely symmetric. Also, without the effects of ambient-mantle SSC to shape and remove parts of the base of the incoming lithosphere in the short-box case, plume-pancake SSC does not produce arch volcanism (Fig. S3). Along these lines, the occurrence of ambient-mantle SSC is critical for widespread secondary volcanism and asymmetry of plume-lithosphere interaction.

For the more realistic large-box models, the pattern of ambient-mantle SSC relative to the location of the plume controls plume-pancake SSC and volcanism. The three cases shown in Figures S2b-d are similar to the reference case shown in Figure S2a. They are governed by the same parameters, and only differ in the position of the hot patch at the base of the model box, which is shifted perpendicular to plate motion in 50 km increments from case to case. Such a setup simulates distinct positions of the plume relative to the pattern of ambient-mantle SSC, since the latter is similar for all cases (being influenced by the model boundaries with SSC downwellings typically organizing at the sides of the box). Figure S2 highlights that the temperature distribution and pattern of convection in the plume pancake are sensitive to the position of the plume relative to

the pattern of SSC. Related effects on magma generation further imply that geographical distributions and geochemical signatures of volcanism are affected by shifts in the position of the plume relative to ambient-mantle SSC. Figures S4-S6 show that such shifts indeed alter rejuvenated volcanic flux (Figs. 3b, S4), average pyroxenite contribution and duration of rejuvenated stage volcanism (Figs. 3b, S4, S6), volcanic flux and geographical distribution of arch volcanism (Figs. 3a, S5), geochemical contrast between the Kea and Loa trends (solid lines in Figs. 3b, S6), and most notably hotspot volcanic flux (numbers in Figs. 3b and S4).

Top-down driven ambient-mantle SSC induces variability of hotspot volcanic flux through the effects of lithospheric thickness undulations (“washboard”) on plume-lithosphere interaction. Both hotspot volcanic flux and the extent of the Kea/Loa geochemical asymmetry are influenced by the position of the plume relative to the washboard (Figs. S4, S6). Thus, they are sensitive to a change in the pattern of ambient-mantle SSC. We speculate that a change in the pattern of SSC upstream of the Hawaiian hotspot as induced by the Molokai Fracture Zone<sup>23,53</sup> or by a recent change in plate motion<sup>51,52</sup> contributed to the sudden appearance of the geochemically asymmetric Kea and Loa sub-chains<sup>11,54</sup> at ~2 Ma and a coeval boost in Hawaiian hotspot volcanism<sup>7,8,26</sup>.

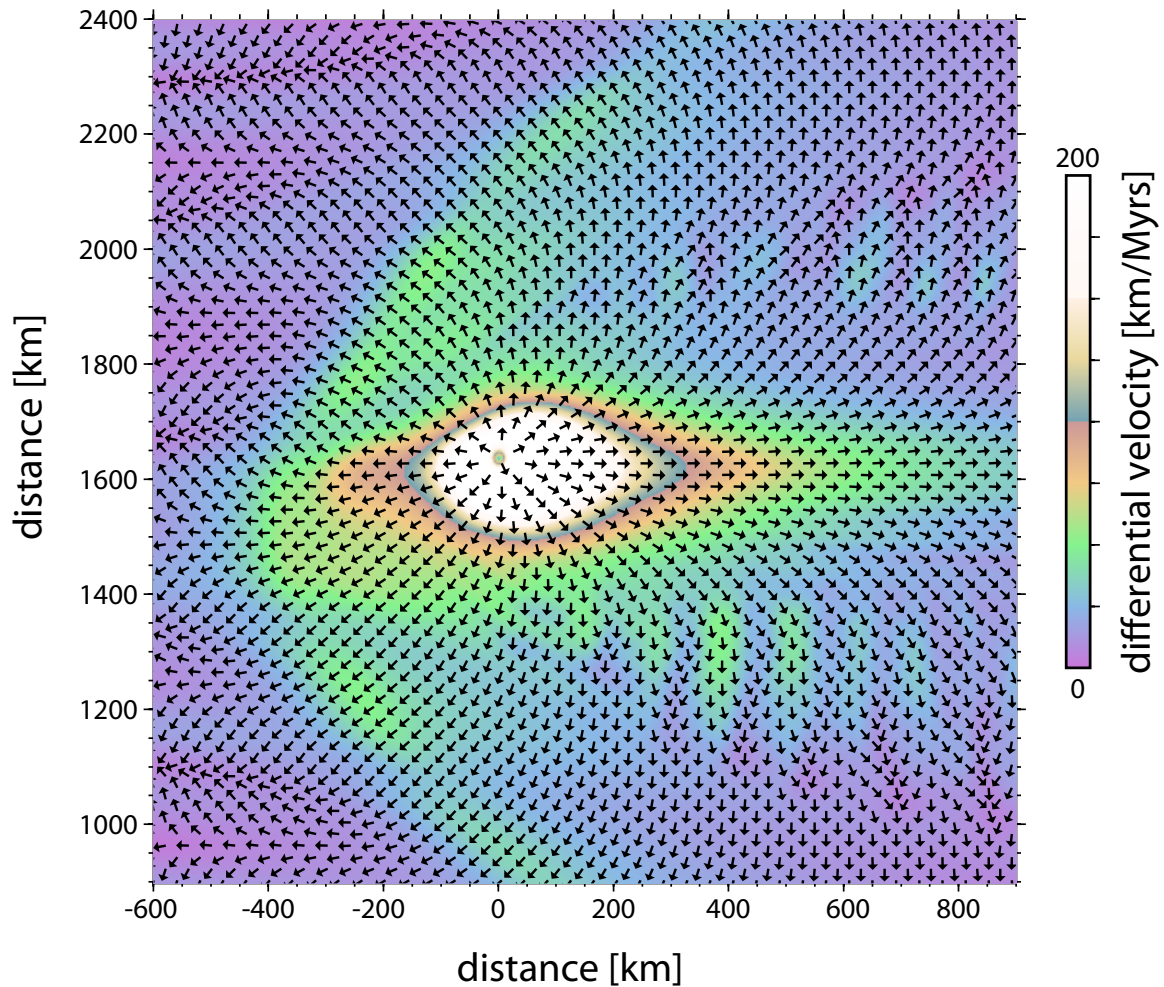
## SC. Controls of melt extraction on secondary volcanism

Figure S7 shows that the predicted total volume of rejuvenated stage volcanism and its duration (or distance, over which it simultaneously occurs) are sensitive to the critical porosity  $\varphi_C$ . For instance, rejuvenated volcanic flux triples when  $\varphi_C$  increases from just 0.8% to 1%. Whereas higher  $\varphi_C$  reduces the fraction of extracted melt in magma produced, the dominating effects in boosting magma production are to increase the mantle buoyancy as more melt is retained, and to keep viscosity low as more water remains in the mantle (cf. equation (S2) and ref. 35). These important effects boost decompression melting by fueling plume-pancake SSC and related erosion at the base of the lithosphere.

Our model predictions can be tested with the geological record of the rejuvenated “Koloa volcanics” on Kauai. Alternative models for the origin of rejuvenated volcanism include decompression melting due to lithospheric flexure<sup>18</sup>, and due to lateral spreading of the plume pancake<sup>3</sup>. Given that widespread rejuvenated volcanism also occurred on the seafloor around Kauai<sup>55</sup>, we neglect major melt focusing towards the island of Kauai during extraction of rejuvenated melts. With this assumption, the lithospheric flexure and pancake spreading models can just account for 6 km<sup>3</sup> and 8 km<sup>3</sup> of rejuvenated volcanism on Kauai, respectively (cf. refs. 3, 18). Therefore, even a combination of both mechanisms is insufficient to explain the large observed volumes of ~60 km<sup>3</sup> of Koloa volcanics<sup>17</sup>. Our models instead predict higher volumes of about 210 km<sup>3</sup>, 170 km<sup>3</sup>,

135 km<sup>3</sup>, 90 km<sup>3</sup> and 55 km<sup>3</sup> over the area of Kauai for critical porosities of 1%, 0.9%, 0.8%, 0.75% and 0.7%, respectively. Depending on the actual ratio of intrusive versus extrusive rejuvenated volcanism, our model predictions for  $\varphi_C \geq 0.75\%$  thus have no difficulty in explaining the large volume of Koloa volcanics.

For the same reasons (above) increasing  $\varphi_C$  boosts rejuvenated volcanism, it also tends to boost volcanic flux of arch volcanism. By fueling SSC on the flanks of the pancake, increasing  $\varphi_C$  from 0.5% to 1% boosts arch volcanic flux from ~550 km/Myrs to ~1000 km/Myrs. To a greater extent, however, SSC on the flanks of the pancake and related arch volcanism are expected to be sensitive to rheological parameters (cf. ref. 24).



**Figure S1. Differential horizontal flow field between the plume pancake and the plate for the reference case.** Arrows denote direction and color denote the amplitude of differential flow as computed by subtracting of plate motion (i.e. 80 km/Myr from left to right) from horizontal flow at 140 km. Arrows pointing to the left/right indicate horizontal flow that is slower/faster than plate motion. The shear associated with this differential motion appears to influence the alignment of SSC in the pancake.

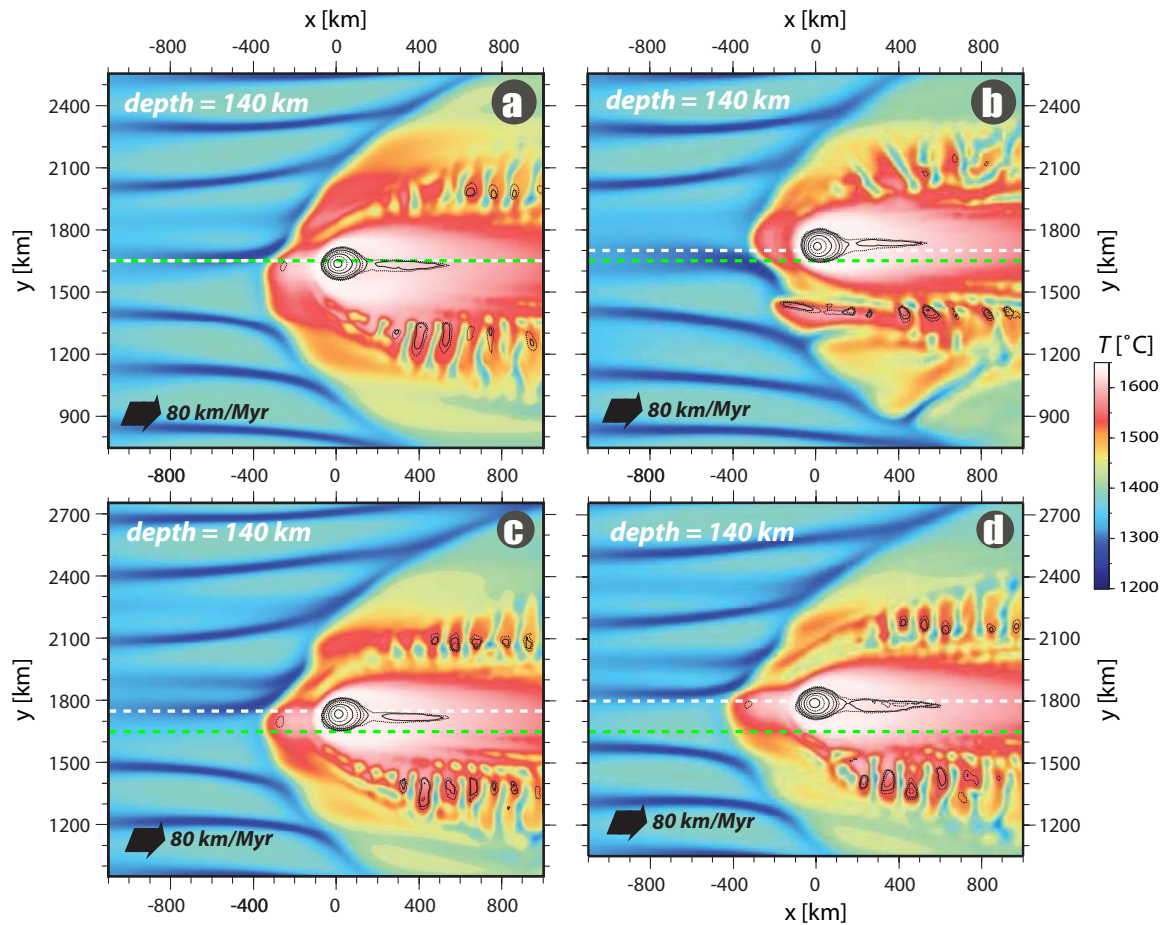


**Figure S2. Horizontal cross-sections of temperature at 140 km depth for different models with contours of the rate of surface volcanism.** From outside to inside, black dashed contours denote 0.01, 0.1, 1, and 10  $\text{km}^3/\text{km}^2/\text{Myr}$  (average over 1000 timesteps). Upwellings and downwellings typically occur where temperatures are relatively high and low, respectively. The light blue and dark blue stripes reveal the pattern of ambient-mantle SSC. Warm colors (and white) are the plume-pancake. The different models simulate different positions of the plume relative to the pattern of ambient-mantle SSC. The position of SSC is influenced by the boundaries of the model box and is similar for all cases; therefore, the model conditions differ only in where the center of the plume is positioned: (a)  $y = 1650$ , (b)  $y = 1700$  km, (c)  $y = 1750$  km, and (d)  $y = 1800$  km. The original position (i.e., at the bottom boundary of the model box) of the plume on the  $y$ -axis is marked by the white dashed line (green dashed line for position of the plume in (a)). The model in (a) is the reference case as also shown in Figs. 2-3. The pattern of SSC in the pancake is sensitive to undulations in lithosphere thickness relative to the plume, which was shaped by SSC in the ambient mantle upstream of the plume.

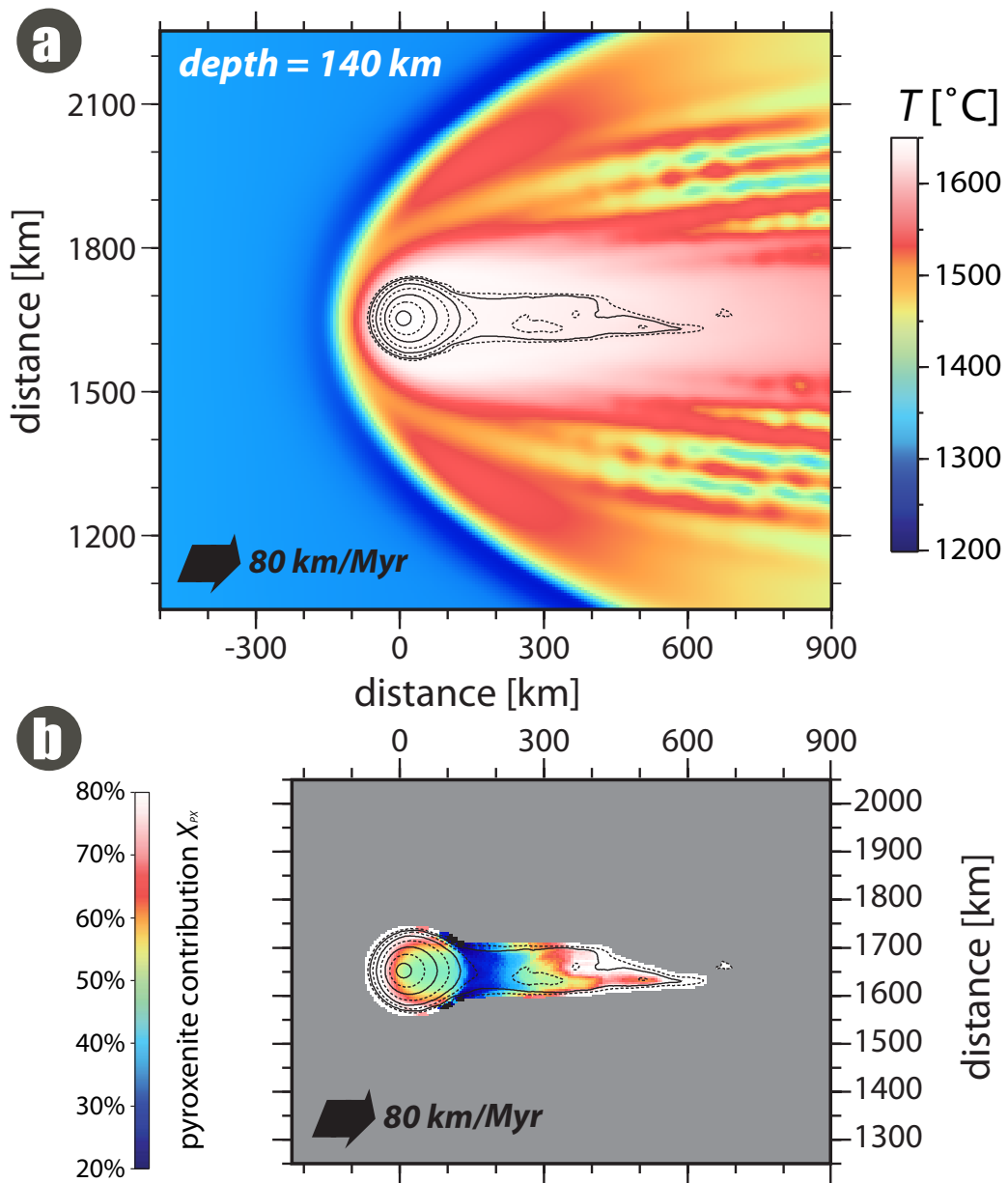


**Figure S3. Model results for case without SSC in the ambient mantle (small-box case).** This case is similar to the reference case, and differs only in box length (2376 km instead of 4818 km). Such a setup prohibits self-organization of ambient-mantle SSC. Panels (a) and (b) show a horizontal cross-section of temperature (cf. Fig. S2), and the origin of volcanism in terms of source lithology (cf. Fig. 3a), respectively. Both panels display contours of surface volcanism (same contour spacing as in Fig. S2). For this case, plume-pancake SSC appears to be insufficient to support arch volcanism.

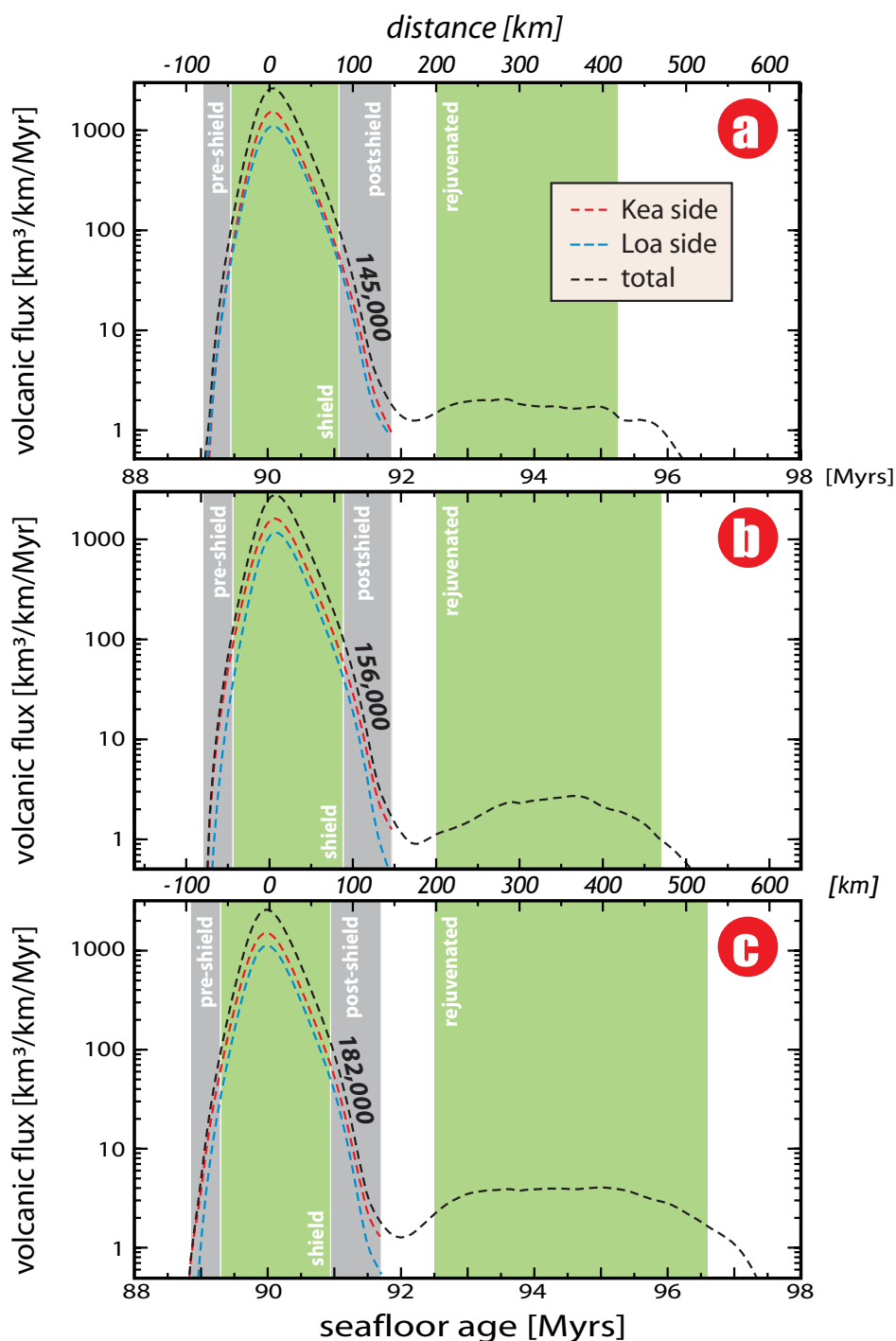


**Figure S4. Volcanic flux versus seafloor age for different positions of the plume relative to the pattern of ambient-mantle SSC.** The 3 cases shown correspond to those in Figs. S2b-d (i.e., the plume is centered at (a)  $y = 1700$  km [cf. Fig. S2b], (b)  $y = 1750$  km [cf. Fig. S2c], and (c)  $y = 1800$  km [cf. Fig. S2d]). Numbers denote total hotspot volcanic flux in  $[\text{km}^3/\text{Myr}]$ . The above curves should be compared to the dashed lines in Fig. 3b, which represent volcanic flux for the reference case with the plume centered at  $y = 1650$  km. Black curves display total volcanic flux. Red and blue curves indicate the volcanic fluxes along the Kea and Loa trends, respectively. The feeding zones for these trends are shown as light grey boxes in Fig. S5. The boundary between the two zones is chosen such that the Kea trend displays  $\sim 25\%$  more volcanism than the Loa-trend—as consistent with the geological record over the past 2 Myrs (ref. 26).

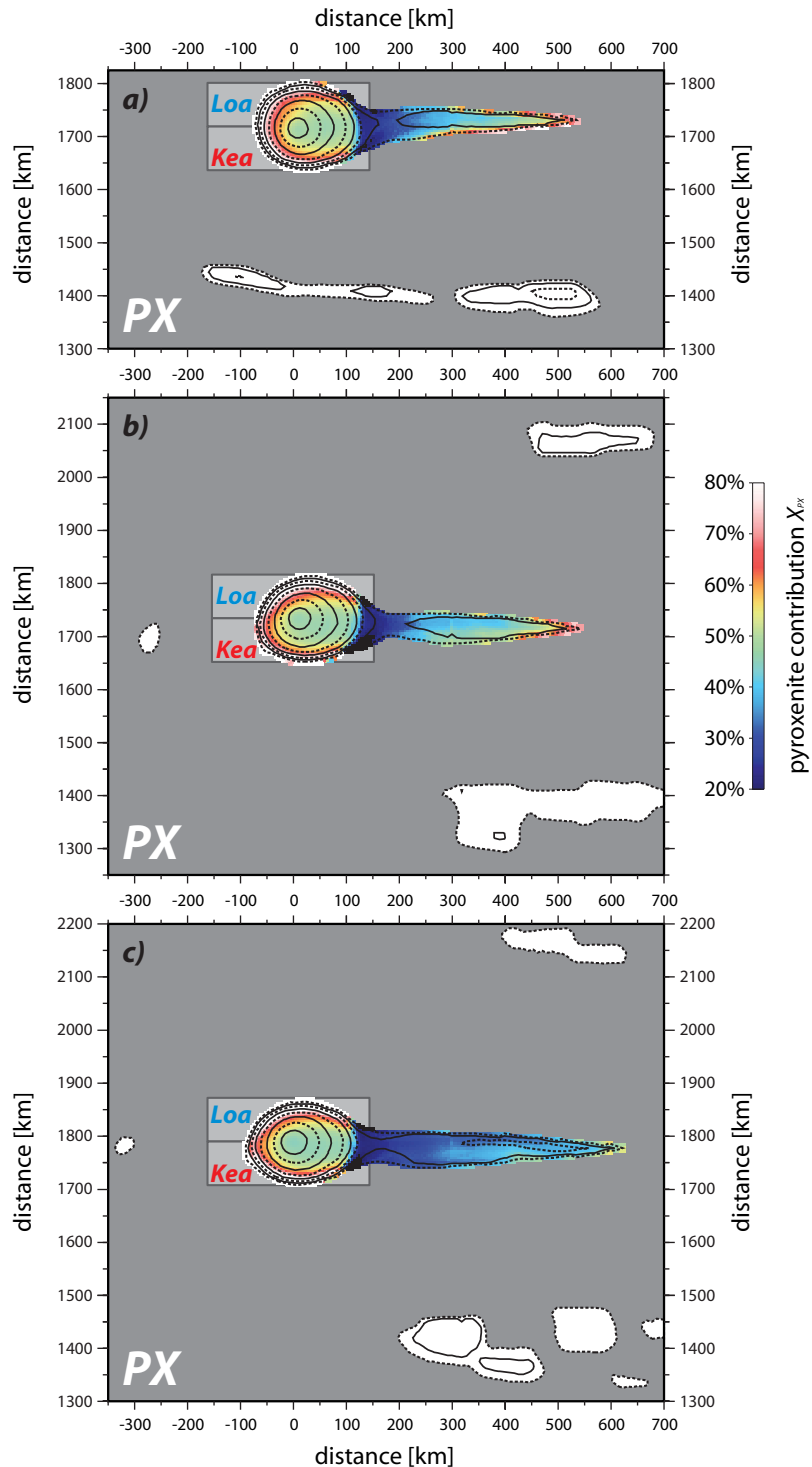


**Figure S5. Composition and volume flux of surface volcanism for different positions of the plume relative to the pattern of ambient-mantle SSC.** The 3 cases (a, b, c) correspond to those as shown in Fig. S4 with the plume centered at (a)  $y = 1700$  km, (b)  $y = 1750$  km, and (c)  $y = 1800$  km, respectively. Colors denote contribution of pyroxenite in surface volcanism; black contours denote the rate of surface volcanism (same contour spacing as in Fig. S2). The above plot should be compared with Fig. 3a that represents the reference case with the plume centered at  $y = 1650$  km.

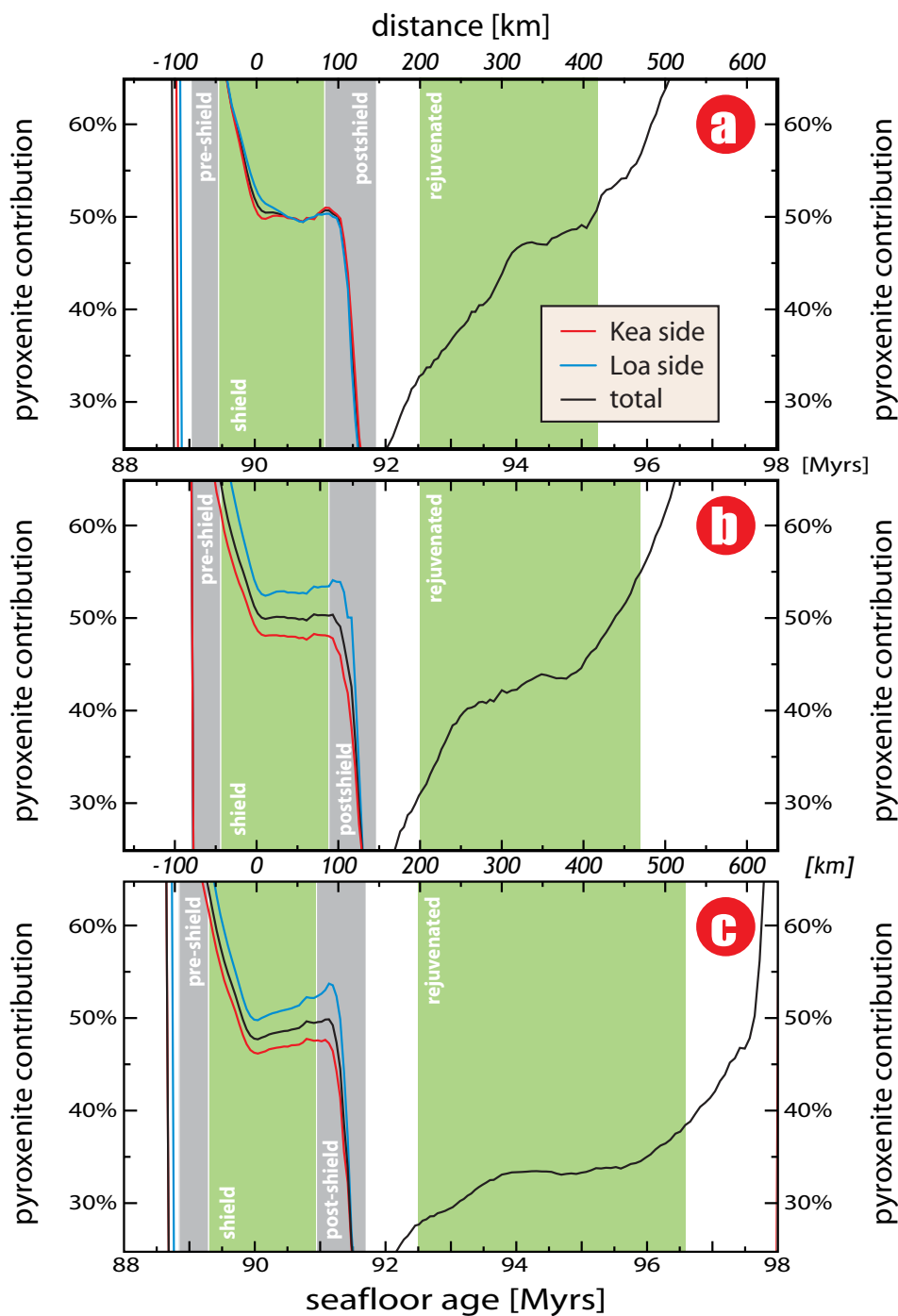


**Figure S6. Pyroxenite contribution versus seafloor age for different positions of the plume relative to the pattern of ambient-mantle SSC.** The 3 cases (a, b, c) correspond to those as shown in Figs. S4-S5 with the plume centered at (a)  $y = 1700$  km, (b)  $y = 1750$  km, and (c)  $y = 1800$  km, respectively. The above curves should be compared to the solid lines in Fig. 3b, which represent pyroxenite contribution for the reference case with the plume centered at  $y = 1650$  km. All cases (including the reference case) except for the case in panel (a) display a distinction in pyroxenite contribution between the Kea and Loa trends of about 5%. This distinction persists through the postshield stage, as does the geochemical distinction between the two trends<sup>10</sup>.

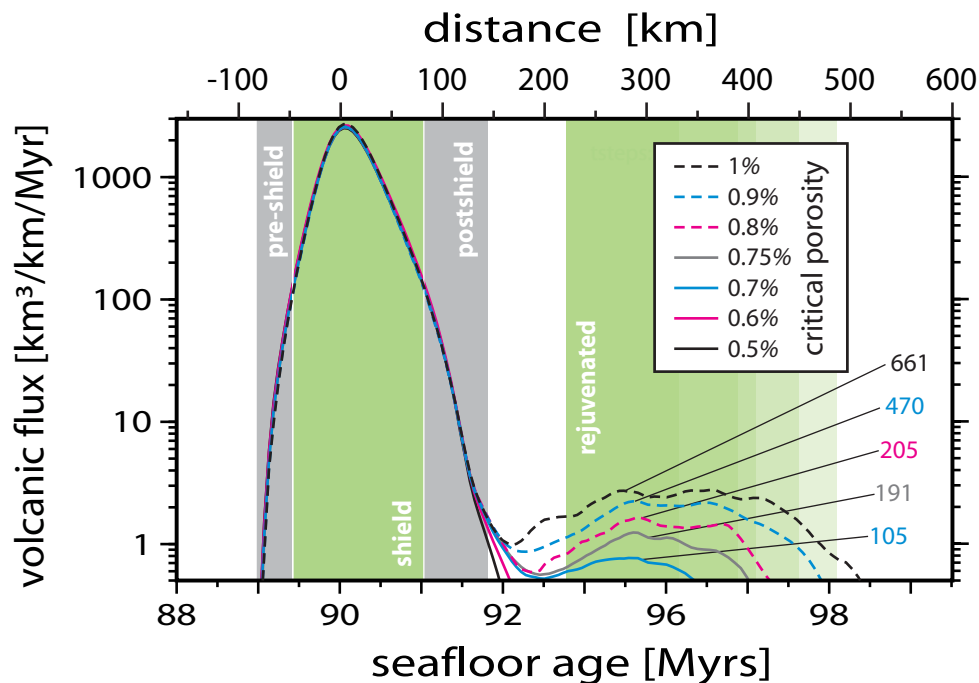


**Figure S7. Volcanic flux versus seafloor age for cases with different critical porosity  $\phi_C$ .** Black dashed line is the same as that in Fig. 3b for the reference case with  $\phi_C = 1\%$ . Numbers denote total rejuvenated volcanic flux in  $\text{km}^3/\text{Myr}$  for the different cases.

## References

- 31 Moresi, L. & Gurnis, M. Constraints On the Lateral Strength Of Slabs From 3-Dimensional Dynamic Flow Models. *Earth Plan. Sci. Lett.* 138, 15-28, (1996).
- 32 Zhong, S., Zuber, M. T., Moresi, L. & Gurnis, M. Role of temperature-dependent viscosity and surface plates in spherical shell models of mantle convection. *J. Geophys. Res.* 105, 11063-11082, (2000).
- 33 Christensen, U. R. & Yuen, D. A. Layered convection induced by phase transitions. *J. Geophys. Res.* 90, 10291-10300, (1985).
- 34 Ballmer, M. D. Small-scale sublithospheric convection - an alternative mechanism for oceanic intraplate volcanism Ph.D. thesis, Diss. ETH No. 18425, ETH Zürich, (2009).
- 35 Ballmer, M. D., van Hunen, J., Ito, G., Bianco, T. A. & Tackley, P. J. Intraplate volcanism with complex age-distance patterns – a case for small-scale sublithospheric convection. *Geochem. Geophys. Geosyst.* 10, Q06015, (2009).
- 36 Schellart, W. P., Stegman, D. R. & Freeman, J. Global trench migration velocities and slab migration induced upper mantle volume fluxes: Constraints to find an Earth reference frame based on minimizing viscous dissipation. *Earth-Science Reviews* 88, 118-144, (2008).
- 37 Allègre, C. J., Hamelin, B. & Dupré, B. Statistical analysis of isotopic ratios in MORB: the mantle blob cluster model and the convective regime of the mantle. *Earth Planet. Sci. Lett.* 71, 71-84, (1984).
- 38 Phipps Morgan, J. Isotope topology of individual hotspot basalt arrays: Mixing curves or melt extraction trajectories? *Geochem. Geophys. Geosyst.* 1, 1003, (1999).

- 39 Hirschmann, M. M. & Stolper, E. M. A possible role for garnet pyroxenite in the origin of the "garnet signature" in MORB. *Contrib. Mineral. Petrol.* **124**, 185-208, (1996).
- 40 Pertermann, M. & Hirschmann, M. M. Partial melting experiments on a MORB-like pyroxenite between 2 and 3 GPa: Constraints on the presence of pyroxenite in basalt source regions from solidus location and melting rate. *J. Geophys. Res.* **108**, 2125, (2003).
- 41 Hirschmann, M. M., Ghiorso, M. S., Wasylenki, L. E., Asimow, P. D. & Stolper, E. M. Calculation of Peridotite Partial Melting from Thermodynamic Models of Minerals and Melts - I - Review of Methods and Comparison with Experiments. *J. Petrol.* **39**, 1091-1115, (1998).
- 42 McKenzie, D. Th-230-U-238 Disequilibrium and the Melting Processes Beneath Ridge Axes. *Earth Planet. Sci. Lett.* **72**, 149-157, (1985).
- 43 Katz, R. F., Spiegelman, M. & Langmuir, C. H. A new parameterization of hydrous mantle melting. *Geochem. Geophys. Geosyst.* **4**, 1073, (2003).
- 44 Zou, H. B. Trace element fractionation during modal and nonmodal dynamic melting and open-system melting: A mathematical treatment. *Geochem. Cosmochem. Acta* **62**, 1937-1945, (1998).
- 45 Karato, S. & Wu, P. Rheology of the upper mantle - a synthesis. *Science* **260**, 771-778, (1993).
- 46 Hirth, G. & Kohlstedt, D. L. Rheology of the upper mantle and mantle wedge: A view from the experimentalists. in: *Inside the subduction factory* (ed J. Eiler) 83-105 (AGU, 2003).
- 47 Hirth, G. & Kohlstedt, D. L. Water in the Oceanic Upper-Mantle - Implications For Rheology, Melt Extraction and the Evolution of the Lithosphere. *Earth Planet. Sci. Lett.* **144**, 93-108, (1996).
- 48 Kohlstedt, D. L. & Zimmerman, M. E. Rheology of partially molten mantle rocks. *Ann. Rev. Earth Planet. Sci.* **24**, 41-62, (1996).
- 49 Richter, F. M. & Parsons, B. On the interaction of two scales of convection in the mantle. *J. Geophys. Res.* **80**, 2529-2541, (1975).
- 50 Clague, D. A. & Dalrymple, G. B. Age and Petrology of Alkalic Postshield and Rejuvenated-Stage Lava from Kauai, Hawaii. *Contrib. Mineral. Petrol.* **99**, 202-218, (1988).
- 51 Wessel, P. & Kroenke, L. W. Ontong Java Plateau and late Neogene changes in Pacific plate motion. *J. Geophys. Res.* **105**, 28255-28277, (2000).
- 52 van Hunen, J. & Zhong, S. Influence of rheology on realignment of mantle convective structure with plate motion after a plate reorganization. *Geochem., Geophys., Geosyst.* **7**, Q08008, (2006).
- 53 Dumoulin, C., Choblet, G. & Doin, M. P. Convective interactions between oceanic lithosphere and asthenosphere: Influence of a transform fault. *Earth Planet. Sci. Lett.* **274**, 301-309, (2008).
- 54 Tanaka, R., Makishima, A. & Nakamura, E. Hawaiian double volcanic chain triggered by an episodic involvement of recycled material: Constraints from temporal Sr-Nd-Hf-Pb isotopic trend of the Loa-type volcanoes. *Earth Planet. Sci. Lett.* **265**, 450-465, (2008).
- 55 Garcia, M. O. *et al.* Widespread Secondary Volcanism Near Northern Hawaiian Islands. *Eos, Transactions, AGU* **89**, 525, (2008).